# Effect of Processing Routes on the Microstructure and Thermoelectric Properties of Half-Heusler TiFe$_{0.5}$Ni$_{0.5}$Sb$_{1-x}$Sn$_x$ (x = 0, 0.05, 0.1, 0.2) Alloys

*Anirudha Karati, Sanyukta Ghosh, Ramesh Chandra Mallik, Rajashekhara Shabadi, B.S. Murty, and U.V. Varadaraju*

Sn-doped TiFe$_{0.5}$Ni$_{0.5}$Sb$_{1-x}$Sn$_x$ (x = 0, 0.05, 0.1, 0.2) were synthesized by vacuum arc melting (VAM). In addition to the half-Heusler phase, secondary phases of Fe–Sb-rich compound and Ti-rich compounds were obtained after VAM. The alloys were then subjected to ball milling for 1 h and 5 h. Ball milling for 1h led to microcrystalline grains, while that for 5 h led to nanocrystalline grains. Ball milling followed by spark plasma sintering (SPS) at 1173 K led to significant reduction in size of secondary phases in the microstructure. The undoped sample exhibited a ZT of 0.008 at 873 K for both 1h and 5h BM-SPS samples.

## 1. Introduction

The ever-increasing demand of fossil fuels coupled with its fast depletion has channeled research interests towards clean, renewable and earth abundant resources. Among the many readily available alternative energy sources, thermoelectricity, which involves heat recovery to produce electricity, has been a topic of intense research over the last few decades. Thermoelectric materials that are used in devices have advantage over conventional heat engines owing to its lack of moving parts, less impact to environment, noiseless operation and high reliability (Ref [1–3]). The efficiency of thermoelectric materials is denoted by the dimensionless figure of merit (ZT), which can be expressed as:

$$ZT = \frac{S^{2\sigma}}{\kappa}T$$

where S represents the Seebeck coefficient, $\sigma$ is the electrical conductivity, $\kappa$ is the thermal conductivity comprising of $\kappa_e$ (electronic) and $\kappa_l$ (lattice), and T is the absolute temperature. For a material to exhibit good thermoelectric property, it should possess high S, high $\sigma$ and low $\kappa$ to obtain a high thermoelectric figure of merit (ZT). However, high $\sigma$ increases the $\kappa_e$ and thus optimization of both $\sigma$ and $\kappa_l$ is required to enhance the overall $\sigma/\kappa$ ratio (Ref [4]). Thermoelectric materials operate in different temperature regimes, and thus there exist different classes of materials such as chalcogenides (Ref [5]), skutterudites (Ref [6]) and Zintl phase compounds (Ref [7]) operating in low- (300-500 K), mid- (500-800 K) and high-temperature (800-1100 K) regimes. One such class of compounds that has demonstrated high ZT in mid- to high-temperature regimes are half-Heusler alloys. Half-Heusler alloys have gained prominence owing to their good mechanical and thermal robustness (Ref [8]), excellent electronic properties due to narrow band gap of ∼1eV, high Seebeck coefficient and high electrical conductivity. Additionally, it is made of elements that are less toxic and more earth abundant (Ref [9]).

Half-Heusler alloys adopt the MgAgAs type of structure crystallizing adopting the space group $F\bar{4}3m$ (Ref [10]). The structure comprises three interpenetrating fcc sub-lattices. Compositions in half-Heusler alloys that have a valence electron count of 18 are found to have the Fermi energy level (E$_f$) to be present in the center of the band structure. Such systems tend to be semiconducting and hence are suitable candidates for thermoelectric applications (Ref [11]). TiNiSn and TiCoSb are the two well-studied systems among half-Heusler alloys (Ref [9]). TiCoSb is an intrinsic n-type semiconductor. It has high room-temperature Seebeck coefficient and electrical resistivity values of − 265 $\mu$V/K and $4.5 \times 10^{-2}$ $\Omega$cm, respectively (Ref [12]). However, it has a very high thermal conductivity of 24 Wm$^{-1}$ K$^{-1}$ at 373 K (Ref [13]). This high thermal conductivity serves to be one of the biggest bottlenecks in the application of half-Heusler alloys as thermoelectric materials. Methods like nanostructuring to introduce grain boundary scattering (Ref [14]), in situ formation of second phase (Ref [15]), ex situ addition of second phase (Ref [16]) and point defects generated due to solid solution formation (Ref [17]) are some of the strategies that have been generally employed to reduce $\kappa$ by reducing the lattice part of thermal conductivity ($\kappa_l$)in half-Heusler alloys. Kim *et al.* reported a much reduced $\kappa_l$ of 2.4

**Anirudha Karati** and **U.V. Varadaraju**, Department of Chemistry, Indian Institute of Technology Madras, Chennai, India; **Sanyukta Ghosh** and **Ramesh Chandra Mallik**, Thermoelectric Materials and Devices Laboratory, Department of Physics, Indian Institute of Science, Bangalore, India; **Rajashekhara Shabadi**, Faculty of Science and Technology, UMET, University of Lille, Villeneuve-d'Ascq, France; **B.S. Murty**, Department of Chemistry, Indian Institute of Technology Madras, Chennai, India; Department of Metallurgical and Materials Engineering, Indian Institute of Technology Madras, Chennai, India; and Indian Institute of Technology Hyderabad, Kandi, India. Contact e-mail: murty@iitm.ac.in.

$Wm^{-1} K^{-1}$ for TiCoSb synthesized by mechanical alloying followed by spark plasma sintering (Ref [18]). Ball milling of cast ingot followed by powder consolidation has led to increased ZT due to grain boundary scattering in $Hf_{0.8}Ti_{0.2}CoSb_{0.8}Sn_{0.2}$ (Ref [19]). It has been further shown that isostructural substitution of Ti in the Zr center leads to improved thermoelectric properties due to increased effective mass and point defect scattering in $Zr_{0.5}Ti_{0.5}CoSb_{0.7}Sn_{0.3}$ (Ref [20]).

Balke *et al.* reported the synthesis of a new half-Heusler alloy, $TiFe_{0.5}Ni_{0.5}Sb$. It was obtained by replacing Co with Fe having an electron less than Co and Ni having an electron greater than Co (Ref [21]). The band structure diagrams of TiFeSb showed the $E_f$ (Fermi level) to be present in the valence band and the material was found to behave like a Curie-Weiss paramagnet (Ref [22]). On the other hand, in the case of the band structure of TiNiSb, the $E_f$ was found to be in the conduction band and the material behaved like a Pauli paramagnet (Ref [22]). The band structure of $TiFe_{0.5}Ni_{0.5}Sb$ shows the presence of Fermi energy level at the center of the valence and conduction bands as per theoretical calculations (Ref [23], [24]). However, because of compositional variations that are commonly encountered during synthesis of half-Heusler compounds, the Fermi level shifts near to conduction band and $TiFe_{0.5}Ni_{0.5}Sb$ ends up exhibiting n-type semiconducting property (Ref [21]). The substitution of Co with Fe and Ni leads to increased electrical conductivity and reduced thermal conductivity in the system when measured at 300 K. This is because while the band gap of $TiFe_{0.5}Ni_{0.5}Sb$ is 0.8 eV (Ref [21]), the band gap of TiCoSb is 0.95 eV (Ref [22]). The reduction in $\kappa$ is attributed to magnetic scattering of phonons by Fe ions, presence of impurity phases and mass fluctuation effects (Ref [21]).

For any thermoelectric device to work, the presence of a p-type and n-type legs having similar thermoelectric and mechanical properties is important. TiCoSb and $TiFe_{0.5}Ni_{0.5}Sb$ exhibit n-type semiconducting property. The introduction of Sn in the Sb center in TiCoSb has led to the generation of p-type thermoelectric materials because of the introduction of holes in the system. This is owing to Sn having an electron less than Sb (Ref [18], [25]). Furthermore, reports have claimed for TiCoSb to exhibit higher ZT at higher temperature (Ref [21]). At present, the high-temperature thermoelectric properties of $TiFe_{0.5}Ni_{0.5}Sb$ have not been reported in the literature. In the present work, synthesis of $TiFe_{0.5}Ni_{0.5}Sb_{1-x}Sn_x (x = 0, 0.05, 0.1, 0.2)$ has been carried out by two routes to see the effect of processing routes on the thermoelectric properties. The alloys are first made by vacuum arc melting followed by (1) Ball Milling for 1 h and spark plasma sintering (1h BM-SPS) and (2) ball milling for 5 h and spark plasma sintering (5h BM-SPS). Subsequently, the thermoelectric properties are measured up to 850 K that gives us an idea about the effects of grain size on the thermoelectric property of these alloys.

## 2. Experimental Section

Ti, Fe, Ni, Sn and Sb powders were weighed in stochiometric ratio and ground, and a green compact was made by applying a uniaxial load of 300 MPa to make a 20-mm diameter pellet. Sb shots were weighed and taken separately. To account for the weight loss of Sb, 5% extra Sb was added. The Sb shots were placed on the copper hearth in the arc melting furnace followed by the pellet (comprising of Ti, Fe, Ni and Sn) on top

of it. The arc melting chamber was pre-evacuated up to $8 \times 10^{-6}$ m-bar pressure, and subsequently high-purity Ar gas was purged into it till it reached $1 \times 10^{-3}$ m-bar pressure. This process was carried out twice. Ti shots, used as getter material, were melted to trap the excess oxygen within the chamber. The loss of Sb, that is generally encountered with owing to its high vapor pressure, was minimized by maintaining a low current throughout the melting process. The buttons were flipped and re-melted 4 times to ensure homogeneity in the sample. The samples were subsequently hand-crushed into powder using a mortar and pestle.

The crushed alloys were made nanocrystalline using Fritsch pulverisette-5 ball mill. The hand-crushed powder was loaded into an 80-mL tungsten carbide (WC) vials containing WC balls. The ball-to-powder weight ratio was kept as 10:1. Toluene was used as process control agent (PCA), and speed of milling was kept to 300 rpm. The cast alloys were milled for 1 h to make microcrystalline powder and for 5 h to make nanocrystalline alloys. In order to consolidate the powder samples, spark plasma sintering (SPS) was carried out using Dr. Sinter Plus. Sintering was carried out at 1173 K at a heating rate of 100 K/min and held at that temperature for 5 minutes. For the 1-h milled samples, a pressure of 60 MPa was applied, while a pressure of 50 MPa was applied for the 5-h milled samples. All the samples exhibited relative density greater than 95 % as determined by Archimedes method. The as-cast alloys were polished to obtain a flat surface and XRD analysis of the same was carried out. XRD analysis was carried out using X'Pert Pro PanAlytical equipment with Cu-K$\alpha$ as X-ray source with a wavelength of 1.5406 Å. The scanning was carried out in the range of 20-90̊ with a scan rate of 0.02 s$^{-1}$ and a time per step of 20 s.

The single-peak profile analysis using pseudo-Voigt function was used for crystallite size analysis from XRD patterns. Rietveld refinement was carried out using FULLPROF software. The phase changes were observed using a SETARAM LabSys evo differential thermal analyzer (DTA) from RT to 600 ºC. The compositions of the alloys were estimated by the mapping mode using an energy dispersive spectroscopy (EDS) unit attached with an Inspect-F field emission scanning electron microscope (FE-SEM) and Quanta 400 (FE-SEM). The Seebeck coefficient (S) and electrical conductivity ($\sigma$) were measured by the differential method and four probe method, respectively, using Linseis LSR-3 from room temperature to 873 K. Thermal diffusivity measurements were investigated using laser flash technique in a Netzsch LFA-427.

## 3. Results and Discussion

### 3.1 Synthesis of Microcrystalline Alloys by Vacuum Arc Melting (VAM)

The XRD patterns of the as-cast alloys are depicted in Fig. [1]. All the alloys exhibited peaks corresponding to the half-Heusler structure crystallizing in $F\bar{4}3m$ structure. No secondary phases were observed in $x = 0$, 0.05 and 0.1 alloys. However, peaks corresponding to full Heusler phase were observed in $x = 0.2$ alloy.

The lattice parameters of the cast alloys were measured using Nelson–Riley function and are as displayed in Table [1]. It was observed that with increasing Sn concentration, there was a

systematic increase in the lattice parameter value in the 1-h and 5-h BM alloys. This could be attributed to Sn having a higher atomic radius of 225 pm as compared to Sb (206 pm). The trend of increase in the lattice parameter is non-monotonic in the case of the SPS pellets. This could be due to the presence of secondary phases present in the SPS pellets. Figure 2 displays the low-magnification images of the cast alloys. In addition to the major grey phase, two other phases, namely black and white, are visible in the microstructure. The major grey phase was found to have a composition that is very similar to the bulk composition in all the samples. The black regions were found to be rich in Ti and exhibit porosities in all the alloys. The white region was found to be rich in Fe/Sb in the pristine sample. In the Sn-doped samples, the white region was found to be rich in Fe/Sb/Sn. The compositions of the individual phases of all the samples are depicted in Table 2.

### 3.2 Synthesis and Consolidation of Microcrystalline Alloys by Ball Milling and Spark Plasma Sintering (1h BM-SPS)

The as-cast alloys were hand-crushed and milled for 1 h to ensure increased homogeneity, and the XRD patterns are as displayed in Fig. 3(a). All the alloys exhibited peaks corresponding to the half-Heusler phase. Additional peaks indexed as full Heusler phase were observed in the 1-h BM powder of the 20% Sn-doped sample. The XRD pattern of the SPS pellets are displayed in Fig. 3(b). All the alloys exhibited single-phase half-Heulser structure without the presence of any secondary phases. The low-magnification images of the SPS pellets
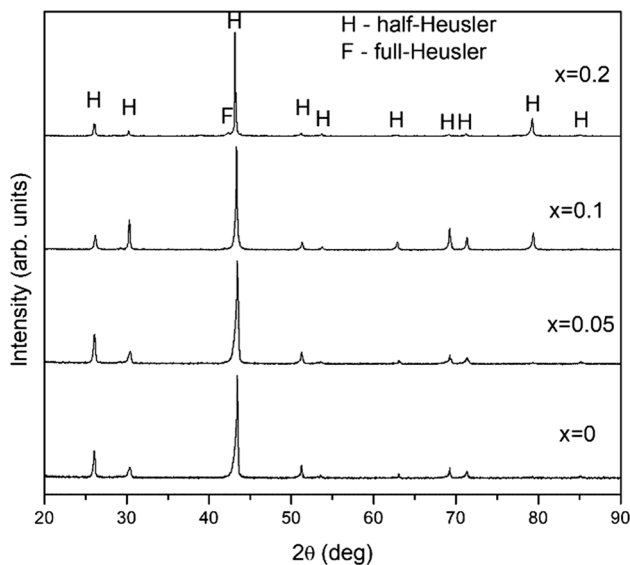


**Fig. 1** XRD patterns of as-cast $TiFe_{0.5}Ni_{0.5}Sb_{1-x}Sn_x$ alloys

confirmed better densification as compared to the cast alloys (Figure S1 of supplementary data). The cast alloys had porosities owing to the high vapor pressure of Sb and reduced boiling point in vacuum that can lead to its evaporation while vacuum arc melting (Ref 26). Furthermore, the size of white region is greatly reduced as there are no white regions observed at low-magnification images (Figure S1 of supplementary data). Thus, combination of BM and SPS significantly reduced the size of the secondary phases. This is because the as-cast alloys are brittle and could be made into fine powder after subjecting it to 1 h of ball milling. This brought about certain reduction in the size of the secondary phases too as they are also brittle in nature (Figure S1 of supplementary data). Additionally, the BM process also helps in dissolution of certain secondary phases as has been observed in our previous reports (Ref 27, 28).

As observed in the as-cast alloy, even the 1-h BM-SPS alloys showed a major grey phase along with two other phases, viz., white and black phases in their microstructure as observed in Fig. 4. The composition of the regions is displayed in Table 3. The bulk composition of all the alloys is similar to the nominal composition. The composition of the grey region is very similar to that of the overall composition. Although the composition of Fe and Ni should be similar, all the samples are found to be slightly richer in Ni. The black region is rich in Ti and corresponds to TiC which forms during the SPS process. Owing to the lower atomic number of Carbon, it could, however, not be estimated accurately. The white region was found to be rich in Fe and Sb in $x = 0$, 0.05 and 0.1 alloys. The white region in $x = 0.2$ alloy was found to be richer in Fe and Sn. Additionally, in all the samples (except $x = 0.2$ alloy) there was significant contribution of Ti owing to the white region being of finer size ($< 1$ $\mu$m) and interaction volume effect coming into play. The composition of $x = 0.2$ alloy in the white region was thus found to be slightly different from the other alloys.

### 3.3 Synthesis and Consolidation of Nanocrystalline Alloys by Ball Milling and Spark Plasma Sintering (5h BM-SPS)

The XRD patterns of the 5-h milled samples are shown in Fig. 5(a). Significant peak broadening was observed after 5 h of milling. The lattice parameter and crystallite size data of the milled alloys are displayed in Tables 1 and 4, respectively. All the alloys exhibited crystallite size below 100 nm. There was no lattice strain observed in all the samples, and hence the data of lattice strain are not included in the table (Table 5). Upon sintering of the milled powder, FeSb phase was also found in addition to the half-Heusler phase from XRD analysis as shown in Fig. 5(b). The Rietveld refinement was carried out on the 5-h milled alloys and is as shown in Figure S2 of supplementary data. The lattice parameter of the as-SPS pellets is shown in
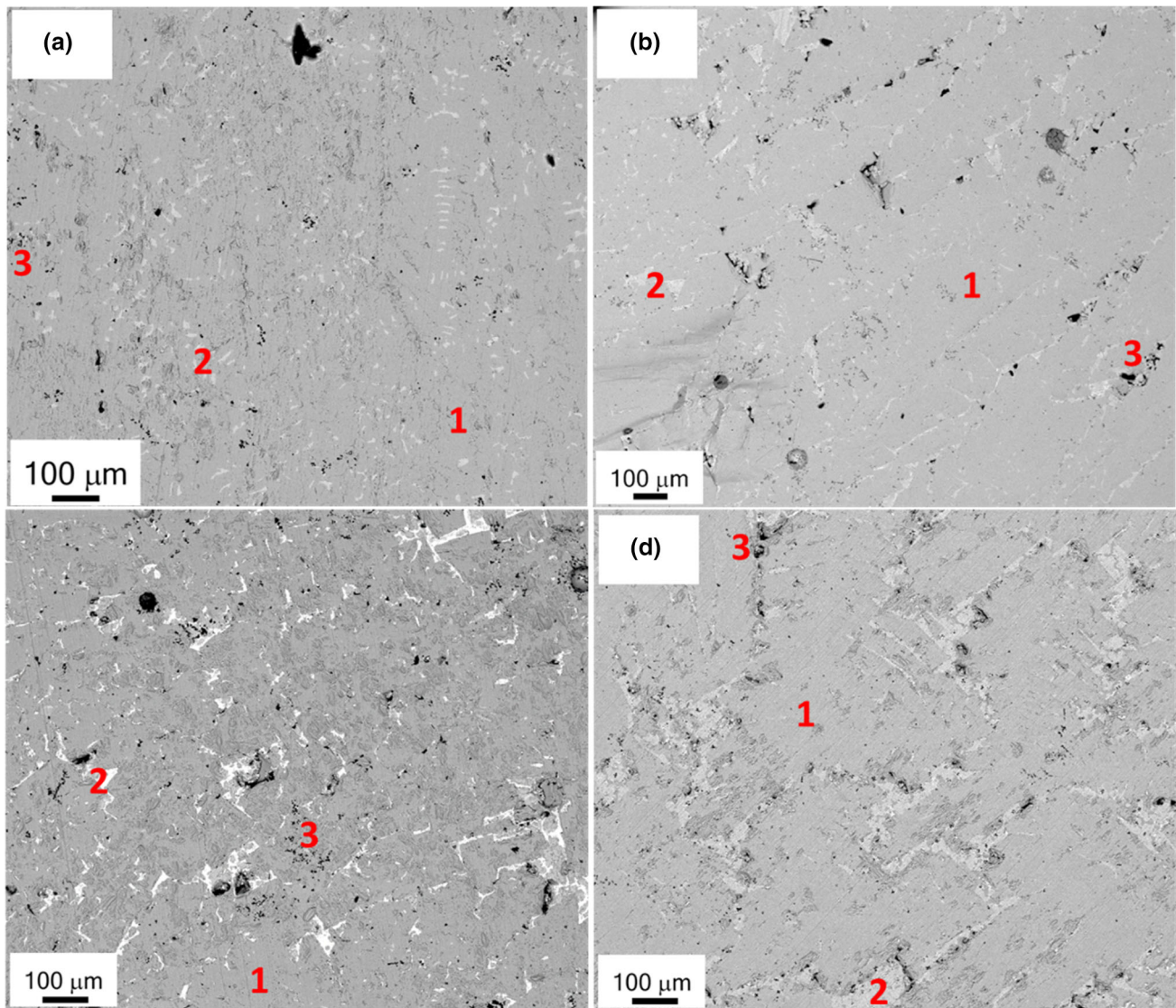
**Table 1** Precision lattice parameter of the alloys based on processing conditions

| Alloy | Cast alloy | 1h BM | 1h BM-SPS | 5h BM | 5h BM-SPS |
|---|---|---|---|---|---|
| | | | Lattice parameter (in nm) based on processing conditions | | |
| $TiFe_{0.5}Ni_{0.5}Sb$ | 0.59150 | 0.59131 | 0.5908 | 0.59133 | 0.59016 |
| $TiFe_{0.5}Ni_{0.5}Sb_{0.95}Sn_{0.05}$ | 0.59154 | 0.59141 | 0.59105 | 0.59143 | 0.59041 |
| $TiFe_{0.5}Ni_{0.5}Sb_{0.9}Sn_{0.1}$ | 0.59159 | 0.59150 | 0.59093 | 0.59154 | 0.59002 |
| $TiFe_{0.5}Ni_{0.5}Sb_{0.8}Sn_{0.2}$ | 0.59191 | 0.59186 | 0.59099 | 0.59167 | 0.59060 |

**Fig. 2** SEM BSE micrographs of as-cast alloys at low magnification showing the presence of 3 regions in (a) $TiFe_{0.5}Ni_{0.5}Sb$, (b) $TiFe_{0.5}Ni_{0.5}Sb_{0.95}Sn_{0.05}$, (c) $TiFe_{0.5}Ni_{0.5}Sb_{0.9}Sn_{0.1}$ and (d) $TiFe_{0.5}Ni_{0.5}Sb_{0.8}Sn_{0.2}$. The labeled phases denote 1 (gray), 2 (white) and 3 (black) phases, respectively

Table 1. The lattice parameter of the alloys was found to be slightly smaller than the milled alloy. This could be attributed to the second-phase (FeSb) formation. The formation of TiC and $Cr_7C_3$ during MA and its increase in volume fraction after SPS are well documented (Ref 24, 25). The absence of Ti leaves behind FeSb. This is greater in the 5-h BM-SPS samples owing to the greater volume fraction of TiC in the 5h BM-SPS samples (Table 6).

The SPS pellets at low magnification showed no porosity as observed in Figure S3 of supplementary data. The high-magnification BSE images of the SPS pellets are shown in Fig. 6. The overall composition of the sample was similar to the expected composition of the alloys. The microstructure revealed a major gray phase, whose composition is similar to that of the nominal alloy composition. In addition, small quantities of black and white regions were observed in the microstructure. The black region is rich in Ti and corresponds to TiC but could not be quantified with precision owing to limitations in the detection of Carbon from EDS. For the sake

of brevity, the composition from two black regions in $TiFe_{0.5}Ni_{0.5}Sb$ is shown in Figure S4 of supplementary data. It is worth noting that owing to the fine size of the grain and the interaction volume effect, the EDS data exhibit certain fraction of the other elements too. Our previous report has established the TiC formation during BM-SPS of HH alloys (Ref 27). The white region that is rich in Fe and Sb is found to be distributed along the particle boundaries in the sample. This could be attributed to the higher diffusivity of the white region for it being rich in Sb, which has a lower melting point. In the Sb-rich side of the Fe-Sb binary phase diagram, there is a presence of a line compound $FeSb_2$ which has a peritectic temperature of 1011 K (Ref 29). All the alloys have slightly higher concentration of Sb in comparison with Fe. The 5-h BM-SPS samples retained their nanocrystallinity as shown in Figure S5 of supplementary data.

**Table 2  SEM-EDS compositional analysis in $TiFe_{0.5}Ni_{0.5}Sb_{1-x}Sn_x$ as-cast pellets (N=3)**

| Alloy | Phase | Ti | Fe | Ni | Sb | Sn |
|---|---|---|---|---|---|---|
| $TiFe_{0.5}Ni_{0.5}Sb$ | Expected | 33.3 | 16.6 | 16.6 | 33.3 | 0 |
| | Overall | 33.6±0.1 | 18.4±0.1 | 17.2±0.1 | 30.7±0.1 | 0 |
| | Grey (1) | 33.4±0.2 | 16.5±0.2 | 18.8±0.3 | 31.2±0.3 | 0 |
| | White (2) | 40.6±1.2 | 8.3±0.7 | 11.2±1.4 | 39.9±0.9 | 0 |
| | Black (3) | 86.7±1.2 | 2.3±0.3 | 5.2±0.6 | 5.8±0.9 | 0 |
| $TiFe_{0.5}Ni_{0.5}Sb_{0.95}Sn_{0.05}$ | Expected | 33.3 | 16.6 | 16.6 | 31.3 | 1.7 |
| | Overall | 34.4±0.3 | 17.8±0.4 | 17.1±0.2 | 29.1±0.1 | 1.7±0.1 |
| | Grey (1) | 34.2±0.1 | 16.6±0.8 | 18.3±0.3 | 29.4±0.2 | 1.5±0.3 |
| | White (2) | 8.0±0.7 | 50.0±1.7 | 1.2±0.7 | 26.3±0.1 | 14.4±0.2 |
| | Black (3) | 75.9±2.9 | 12.2±0.9 | 0.2±0.0 | 11.6±0.8 | 2.2±1.2 |
| $TiFe_{0.5}Ni_{0.5}Sb_{0.9}Sn_{0.1}$ | Expected | 33.3 | 16.6 | 16.6 | 30 | 3.3 |
| | Overall | 34.0±0.4 | 17.8±0.4 | 17.0±0.3 | 28.0±0.1 | 3.2±0.5 |
| | Grey (1) | 35.3±0.4 | 15.6±0.9 | 16.9±0.7 | 29.0±0.2 | 3.2±0.2 |
| | White (2) | 34.7±3.1 | 29.6±4.4 | 2.2±0.9 | 30.6±2.3 | 4.5±0.5 |
| | Black (3) | 95.1±2.3 | 1.8±0.9 | 0.2±0.0 | 0.7±0.2 | 2.2±1.0 |
| $TiFe_{0.5}Ni_{0.5}Sb_{0.8}Sn_{0.2}$ | Expected | 33.3 | 16.6 | 16.6 | 26.7 | 6.6 |
| | Overall | 34.0±0.1 | 18.1±0.2 | 17.8±0.0 | 24.3±0.2 | 5.9±0.3 |
| | Grey (1) | 33.9±0.8 | 14.7±0.1 | 21.1±0.5 | 25.8±0.4 | 4.5±0.1 |
| | White (2) | 36.5±0.9 | 24.3±3.1 | 4.5±2.1 | 26.1±2.7 | 8.6±2.6 |
| | Black (3) | 79.1±0.0 | 5.1±0.1 | 5.7±0.4 | 8.6±0.1 | 1.6±0.1 |
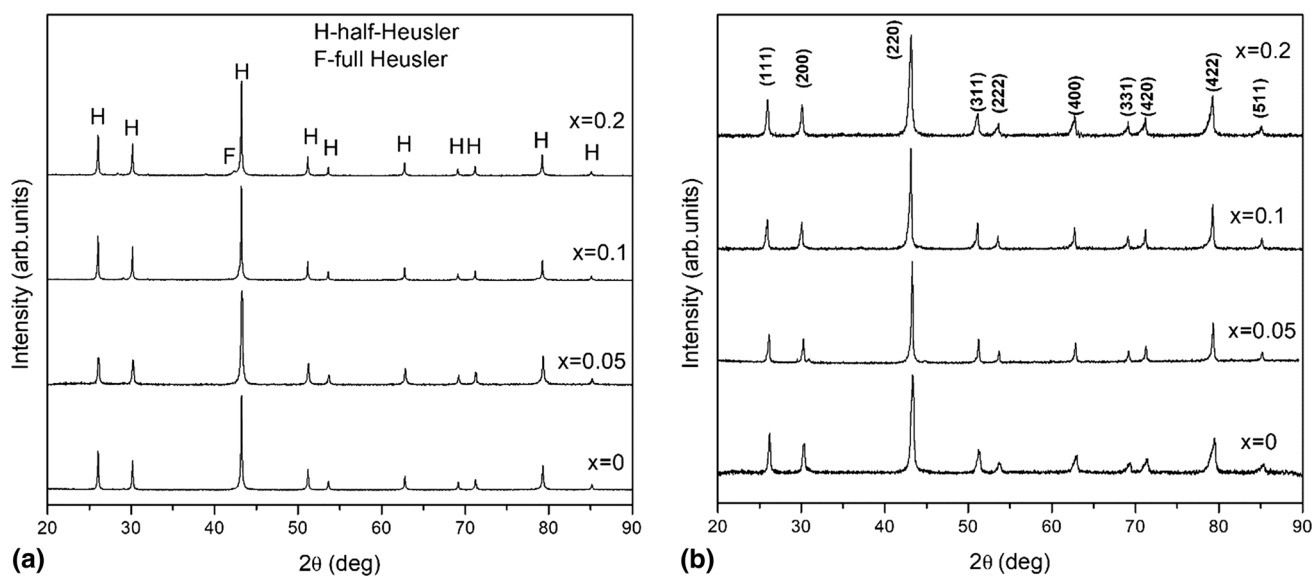


**Fig. 3**  XRD patterns of 1h (a) BM alloys, (b) BM-SPS $TiFe_{0.5}Ni_{0.5}Sb_{1-x}Sn_x$ alloys

### 3.4 Transport Properties of 1h BM-SPS Samples

The Seebeck coefficient as a function of temperature for the 1-h BM-SPS samples are displayed in Fig. 7(a). The S value for the pristine sample is negative at every temperature. This indicates that the alloy is an n-type semiconductor. Although the band structure of $TiFe_{0.5}Ni_{0.5}Sb$ predicts the sample to have the $E_f$ at the center of the band gap, minor variations in Fe and Ni content can shift the $E_f$ closer to the valence band or conduction band respectively (Ref 21). As can be observed from Table 3, all the samples exhibited a slight excess of Ni in comparison to Fe. The n-type character in all the samples except $x = 0.2$ alloy corroborates with that predicted in literature of Ni excess $TiFe_{0.5}Ni_{0.5}Sb$ alloys exhibiting n-type semiconducting behavior. Additionally, the Seebeck coefficient of the pristine sample obtained at room temperature is lower than the reported value (Ref 21). It is also lower than that reported for TiCoSb (Ref 13). The lower values can be attributed to minor compositional variation by way of (1) loss of Sb, (2) presence of Fe-Sb-type secondary phase, and (3) TiC as a secondary phase. The loss of Sb has been reported to alter the thermoelectric properties in similar materials (Ref 30). The change in polarity in the Seebeck coefficient value has been reported in the literature and has been attributed to a change in stoichiometry and reduced structural disorder (Ref 12, 13). Additionally, there is a slight difference in the composition of the $x = 0.2$ alloy and the white region is rich in Fe, Sn and Sb in this alloy. This could also be a reason for $x = 0.2$ alloy to be
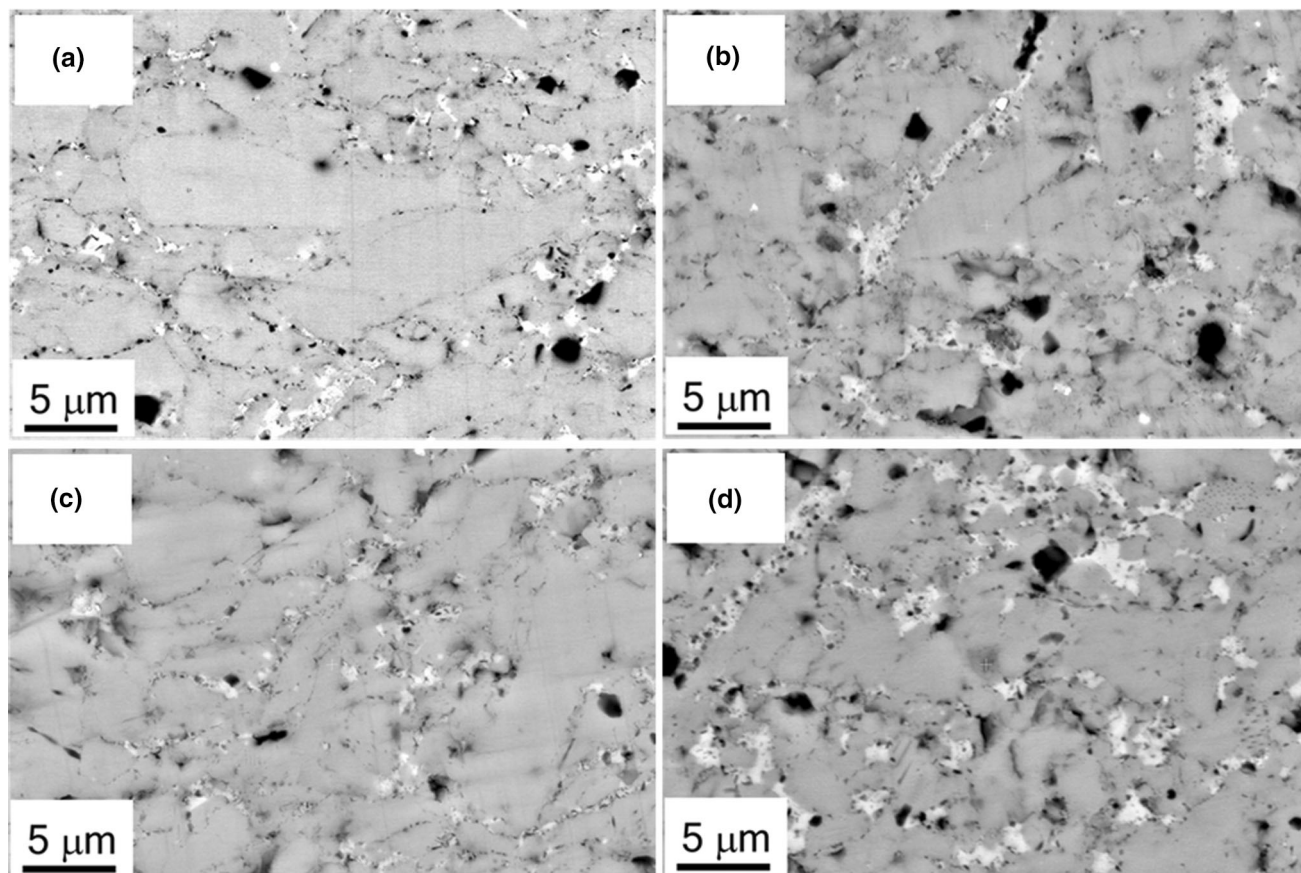
**Fig. 4** SEM micrographs of 1h BM-SPS pellets at high magnification showing second phase (white) in (a) $TiFe_{0.5}Ni_{0.5}Sb$, (b) $TiFe_{0.5}Ni_{0.5}Sb_{0.95}Sn_{0.05}$, (c) $TiFe_{0.5}Ni_{0.5}Sb_{0.9}Sn_{0.1}$ and (d) $TiFe_{0.5}Ni_{0.5}Sb_{0.8}Sn_{0.2}$

**Table 3  SEM-EDS compositional analysis in $TiFe_{0.5}Ni_{0.5}Sb_{1-x}Sn_x$ 1h BM-SPS pellets (N=3)**

| Alloy | Phase | Element | | | | |
|---|---|---|---|---|---|---|
| | | Ti | Fe | Ni | Sb | Sn |
| $TiFe_{0.5}Ni_{0.5}Sb$ | Expected | 33.3 | 16.6 | 16.6 | 33.3 | 0 |
| | Overall | 33.9±0.2 | 17.6±0.2 | 15.8±0.1 | 32.9±0.1 | 0 |
| | Grey | 33.3±0.3 | 16.2±0.1 | 18.0±0.1 | 32.5±0.3 | 0 |
| | White | 21.3±0.3 | 26.5±0.2 | 15.1±0.2 | 37.1±0.1 | 0 |
| | Black | 59.8±0.4 | 10.2±0.2 | 9.5±0.7 | 20.5±0.3 | 0 |
| $TiFe_{0.5}Ni_{0.5}Sb_{0.95}Sn_{0.05}$ | Expected | 33.3 | 16.6 | 16.6 | 31.3 | 1.7 |
| | Overall | 33.6±0.3 | 17.3±0.3 | 15.9±0.3 | 31.0±0.1 | 2.3±0.2 |
| | Grey | 33.7±0.3 | 15.4±0.4 | 18.4±0.4 | 30.9±0.1 | 1.5±0.1 |
| | White | 17.5±1.1 | 28.6±0.3 | 13.3±0.9 | 31.6±1.5 | 9.0±1.6 |
| | Black | 54.7±0.9 | 12.0±0.6 | 9.8±0.1 | 21.0±0.2 | 2.5±0.2 |
| $TiFe_{0.5}Ni_{0.5}Sb_{0.9}Sn_{0.1}$ | Expected | 33.3 | 16.6 | 16.6 | 30 | 3.3 |
| | Overall | 33.5±0.2 | 17.1±0.2 | 16.1±0.1 | 29.9±0.1 | 3.4±0.1 |
| | Grey | 33.4±0.5 | 15.3±1.0 | 18.6±0.9 | 30.3±0.9 | 2.4±0.9 |
| | White | 21.5±1.2 | 25.4±1.0 | 14.4±0.5 | 29.6±0.7 | 9.2±1.3 |
| | Black | 75.9±2.2 | 5.9±0.6 | 5.7±0.6 | 11.2±0.9 | 1.3±0.1 |
| $TiFe_{0.5}Ni_{0.5}Sb_{0.8}Sn_{0.2}$ | Expected | 33.3 | 16.6 | 16.6 | 26.7 | 6.6 |
| | Overall | 33.0±0.2 | 17.5±0.1 | 16.4±0.2 | 26.6±0.3 | 6.5±0.1 |
| | Grey | 33.3±0.2 | 15.1±0.6 | 18.9±0.5 | 27.6±0.4 | 5.1±0.3 |
| | White | 6.2±1.2 | 47.8±2.0 | 8.7±0.5 | 13.7±0.9 | 23.6±1.1 |
| | Black | 37.9±1.2 | 23.8±0.7 | 9.8±0.4 | 17.0±0.8 | 11.5±0.5 |

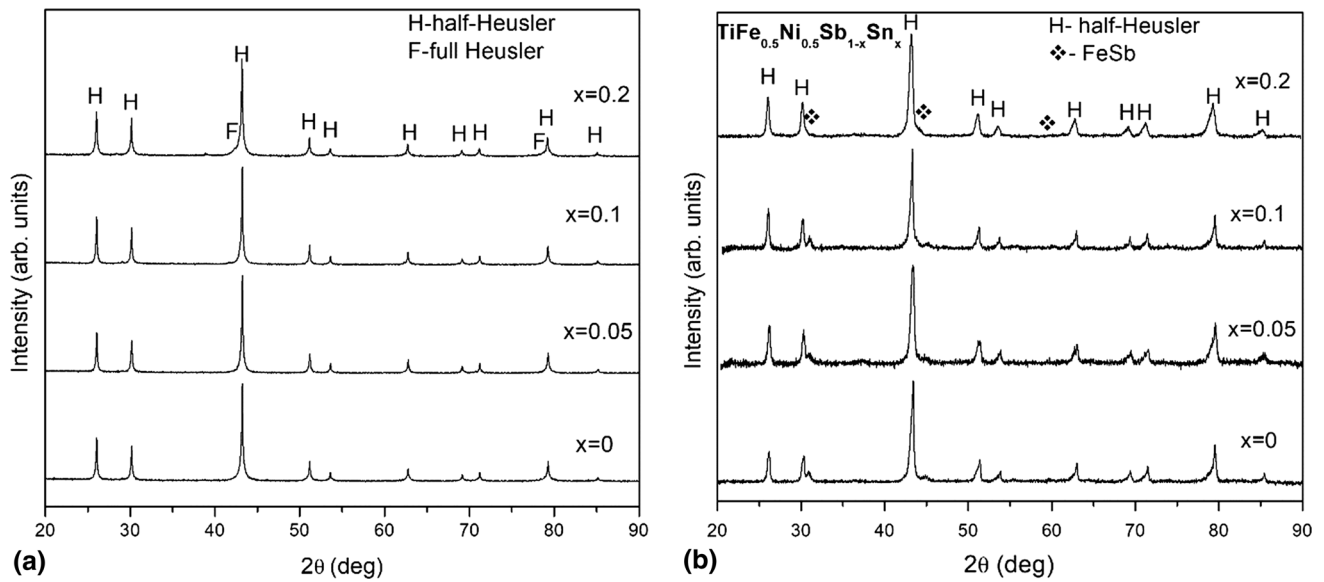**Fig. 5** XRD patterns of 5h (a) BM alloys, (b) BM-SPS $TiFe_{0.5}Ni_{0.5}Sb_{1-x}Sn_x$ alloys

**Table 4** Crystallite size of the alloys based on processing conditions

| Alloy | Crystallite size (in nm) of half-Heusler phase | |
| --- | --- | --- |
| | 5h BM | 5h BM-SPS |
| $TiFe_{0.5}Ni_{0.5}Sb$ | 23±2 | 28±3 |
| $TiFe_{0.5}Ni_{0.5}Sb_{0.95}Sn_{0.05}$ | 29±3 | 35±4 |
| $TiFe_{0.5}Ni_{0.5}Sb_{0.9}Sn_{0.1}$ | 29±2 | 38±3 |
| $TiFe_{0.5}Ni_{0.5}Sb_{0.8}Sn_{0.2}$ | 30±1 | 40±2 |

**Table 5** SEM-EDS compositional analysis in $TiFe_{0.5}Ni_{0.5}Sb_{1-x}Sn_x$ 5h BM-SPS pellets (N = 3)

| Alloy | Phase | Element | | | | |
| --- | --- | --- | --- | --- | --- | --- |
| | | Ti | Fe | Ni | Sb | Sn |
| $TiFe_{0.5}Ni_{0.5}Sb$ | Expected | 33.3 | 16.6 | 16.6 | 33.3 | 0 |
| | Overall | 36.1±0.5 | 16.9±0.2 | 15.6±0.1 | 31.4±0.2 | 0 |
| | Grey | 33.5±0.3 | 15.6±0.2 | 18.2±0.4 | 32.6±0.8 | 0 |
| | White | 20.4±1.0 | 25.6±1.5 | 16.2±1.2 | 37.8±0.6 | 0 |
| | Black | 88.5±2.4 | 2.5±0.8 | 2.2±0.6 | 6.7±1.1 | 0 |
| $TiFe_{0.5}Ni_{0.5}Sb_{0.95}Sn_{0.05}$ | Expected | 33.3 | 16.6 | 16.6 | 31.3 | 1.7 |
| | Overall | 36.4±0.1 | 16.4±0.1 | 15.6±0.1 | 29.8±0.3 | 1.9±0.1 |
| | Grey | 34.1±0.9 | 15.4±0.5 | 18.3±0.1 | 31.1±0.4 | 1.4±0.7 |
| | White | 12.9±0.6 | 27.1±0.1 | 17.5±0.8 | 38.0±0.8 | 5.0±0.7 |
| | Black | 46.1±2.3 | 13.4±0.7 | 13.0±0.5 | 25.7±0.7 | 1.8±0.4 |
| $TiFe_{0.5}Ni_{0.5}Sb_{0.9}Sn_{0.1}$ | Expected | 33.3 | 16.6 | 16.6 | 30 | 3.3 |
| | Overall | 36.2±0.8 | 16.6±0.3 | 15.4±0.2 | 28.7±0.6 | 3.1±0.5 |
| | Grey | 31.9±0.2 | 15.4±0.1 | 19.5±0.6 | 30.4±0.3 | 2.8±0.2 |
| | White | 14.8±0.1 | 29.5±0.7 | 15.6±0.1 | 31.2±1.4 | 9.0±2.1 |
| | Black | 67.8±2.1 | 9.6±0.5 | 7.3±0.4 | 9.5±0.7 | 5.8±0.6 |
| $TiFe_{0.5}Ni_{0.5}Sb_{0.8}Sn_{0.2}$ | Expected | 33.3 | 16.6 | 16.6 | 26.7 | 6.6 |
| | Overall | 36.6±0.3 | 16.4±0.1 | 15.5±0.3 | 26.7±0.2 | 4.8±0.3 |
| | Grey | 33.3±1.9 | 15.6±0.4 | 18.2±1.7 | 29.1±1.7 | 3.7±1.2 |
| | White | 32.9±0.4 | 19.2±0.4 | 14.8±0.6 | 24.4±1.0 | 8.7±1.7 |
| | Black | 76.1±2.2 | 5.6±0.4 | 5.9±0.6 | 10.6±1.0 | 1.9±0.2 |

**Table 6  Image analysis of SPS pellets showing volume fraction of white phase (N = 5)**

| Alloy | White region | | Black region | |
|---|---|---|---|---|
| | 1h BM-SPS | 5h BM-SPS | 1h BM-SPS | 5h BM-SPS |
| $TiFe_{0.5}Ni_{0.5}Sb$ | 2.2±0.5 | 3.1±0.3 | 1.7±0.2 | 3.6±0.1 |
| $TiFe_{0.5}Ni_{0.5}Sb_{0.95}Sn_{0.05}$ | 2.2±0.3 | 5.1±0.1.4.1 | 1.8±0.3 | 4.1±0.1 |
| $TiFe_{0.5}Ni_{0.5}Sb_{0.9}Sn_{0.1}$ | 2.9±0.2 | 5.5±0.4 | 2.1±0.3 | 4.5±0.1 |
| $TiFe_{0.5}Ni_{0.5}Sb_{0.8}Sn_{0.2}$ | 4.8±0.1 | 6.2±0.8 | 2.7±0.4 | 5.9±0.2 |
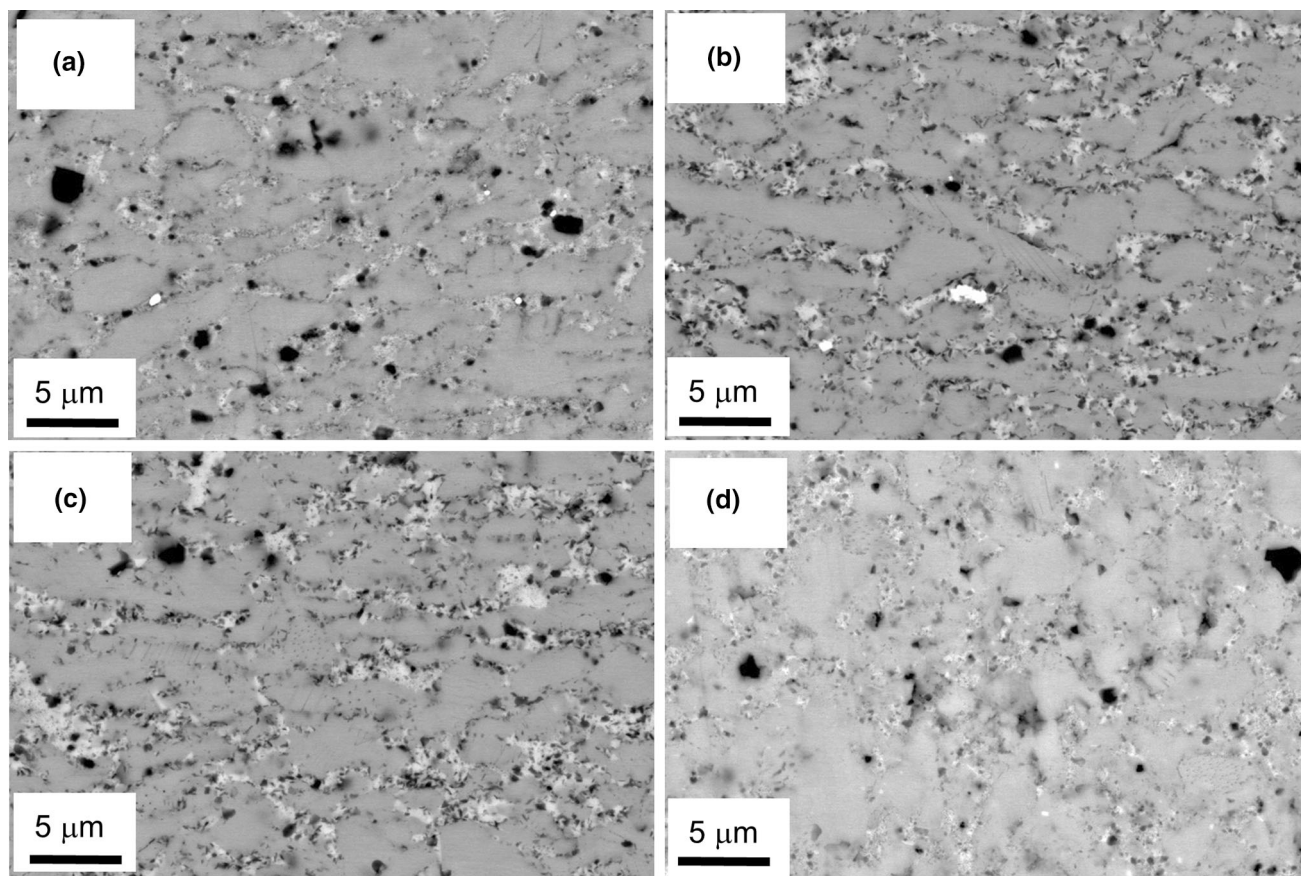


**Fig. 6** SEM micrographs of 5h BM-SPS pellets at high magnification showing second phase (white) in (a) $TiFe_{0.5}Ni_{0.5}Sb$, (b) $TiFe_{0.5}Ni_{0.5}Sb_{0.95}Sn_{0.05}$, (c) $TiFe_{0.5}Ni_{0.5}Sb_{0.9}Sn_{0.1}$ and (d) $TiFe_{0.5}Ni_{0.5}Sb_{0.8}Sn_{0.2}$

exhibiting a change in polarity to become a p-type semiconductor.

The electrical conductivity of the pristine sample is the least across all range of temperature of measurement as shown in Fig. 7(b). The conductivity increases with temperature for all the samples. This is a trend observed commonly in non-degenerate semiconductors. The change in slope increases progressively with increasing Sn content. This can be attributed to the increase in metallic character in the alloys. In the case of Sn-doped samples, there is an abrupt transition in electrical conductivity in the temperature range of 550-750 K. The sudden change in conductivity value in the heating cycle can be attributed to the presence of the secondary phase (Table 3). This is because the half-Heusler phase is stable up to its melting point. In order to confirm the effect of the secondary white region on this sudden increase, DTA studies were carried out for the $x = 0.05$ and $x = 0.2$ samples as shown in Figure S6 of

supplementary data. Endothermic peak with an onset temperature of 643 and 694 K was observed in the case of $x = 0.05$ and $x = 0.2$ alloys, respectively. However, the nature of phase transformation that is responsible for this is hard to decipher. This is because the low-volume fraction of secondary white region goes undetected in XRD. However, it is worth noting that although the phase goes undetected in XRD, the white phase could be established using EDS. Similar transition in electrical conductivity has been reported in Sn-doped TiCoSb. This is attributed to the presence of CoSb which is present as a secondary phase (Ref 18).

The power factor of the pristine sample reached 0.056 $mWm^{-1}\ K^{-2}$ at 737 K as shown in Fig. 7(c). With increasing Sn content, there was decrease in the power factor. This is because the decrease in S value dominates over the increase in the κ value. Owing to higher Seebeck coefficient in the heating
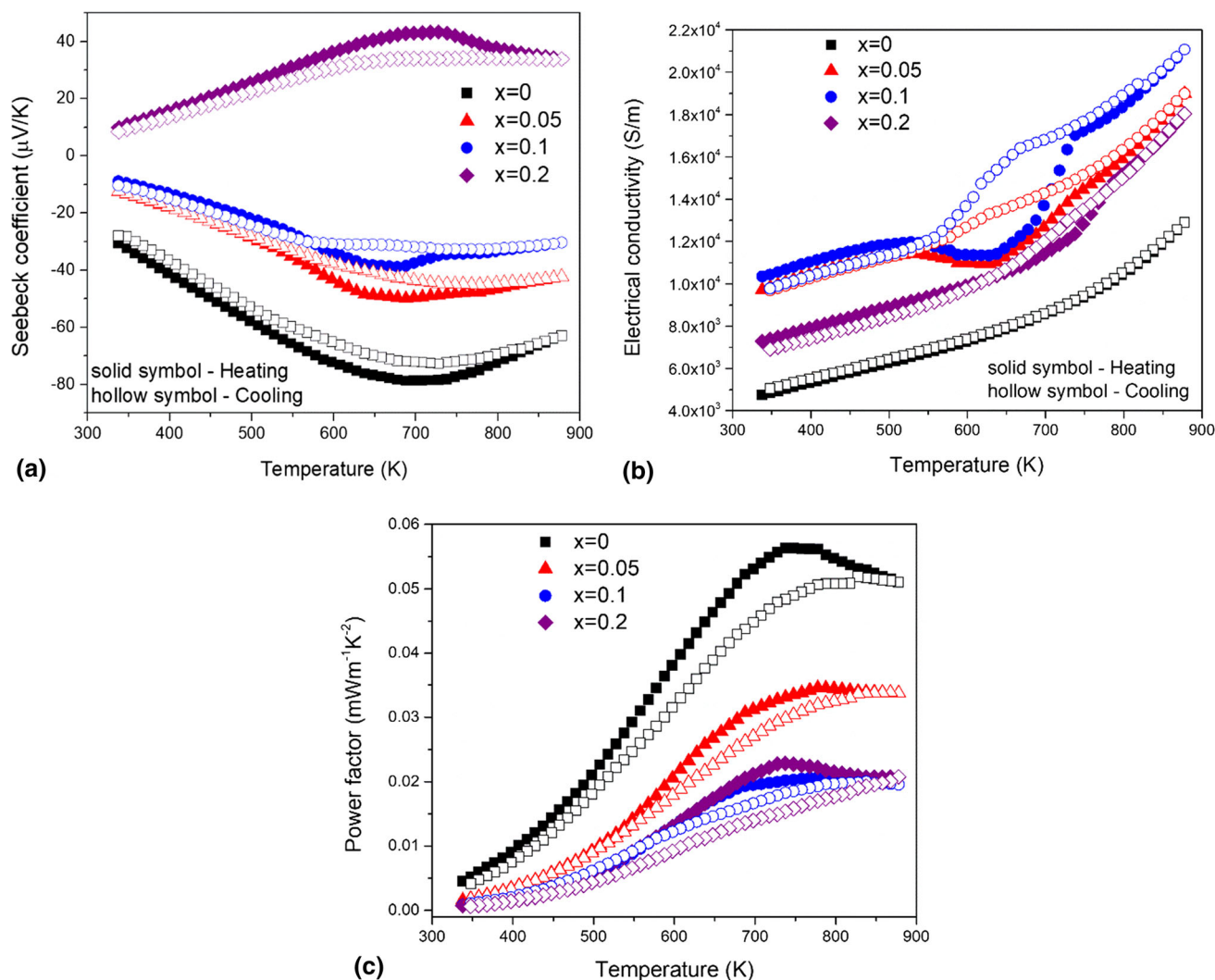
**Fig. 7** (a) Seebeck coefficient, (b) electrical conductivity and (c) power factor of 1h BM-SPS $TiFe_{0.5}Ni_{0.5}Sb_{1-x}Sn_x$

cycle of the samples, the net power factor in the heating cycle is greater than in the cooling cycle.

The total thermal conductivity of all the alloys exhibit Umklapp type of scattering as shown in Fig. 8(a). The $\kappa$ decreases with the increase in temperature for all the alloys. The $\kappa$ for TiCoSb is reported to be 24 $Wm^{-1} K^{-1}$ at 350 K (Ref 13). The k of the pristine sample is, however, much higher (9.2 $Wm^{-1} K^{-1}$) than that reported by Balke *et al.* (4 $Wm^{-1} K^{-1}$) (Ref 21). Additionally, with increasing Sn concentration there was an increase in the $\kappa$ of all the samples which was contrary to that reported earlier (Ref 13). In order to see the contribution of the electronic ($\kappa_e$) and lattice ($\kappa_l$) towards $\kappa$, they were calculated for all the samples. The Lorenz number (L) has been calculated by considering acoustic phonon scattering model as reported before (Ref 31). The room temperature $\kappa_e$ values are demonstrated in Figure 8(b). The $\kappa_e$ for all the samples is $<0.1$ $Wm^{-1} K^{-1}$ at 350 K. The $\kappa_e$ is in the range of 0.25-0.45 $Wm^{-1} K^{-1}$ at 873 K for all the samples which is slightly higher than that reported for TiCoSb (Ref 13). The $\kappa_e$ contributes less than 10% to $\kappa$. Thus, the major contribution to $\kappa$ is due to $\kappa_l$ as demonstrated in Fig. 8(c). Owing to the grain size being large in the 1h BM-SPS pellets, the $\kappa_l$ is high for all the samples. Increase in Sn concentration leads to increased volume fraction

of secondary phases which in turn leads to an increase in $\kappa_l$ and $\kappa$. $FeSb_2$ and TiC are both known to have high $\kappa$ value with TiC known to exhibit increase in $\kappa$ value with the increase in temperature (Ref 32, 33).

The plot of ZT as a function of increasing temperature is displayed in Fig. 8(d). The pristine sample exhibits a maximum ZT of 0.0078 at 873 K. With increasing Sn concentration, there is a simultaneous decrease in power factor and thermal conductivity. This in turn leads to a monotonic decrease in the ZT value with increasing Sn concentration. This value is, however, higher than that reported by Balke *et al.* at 400 K for the pristine sample (Ref 21).

### 3.5 Transport Properties of 5h BM-SPS Samples

The Seebeck coefficient as a function of temperature is displayed in Fig. 9(a). There is an increase in Seebeck coefficient for all the samples with increasing temperature. The Seebeck coefficient for all the samples is lower than the 1h BM-SPS samples. This can be attributed to the increased volume fraction of the secondary phases (Table 6). The Seebeck coefficient decreases with increasing Sn concentration. This can be attributed to the increase in secondary phase formation as shown in Fig. 6 and Table 6. However, the exact composition of
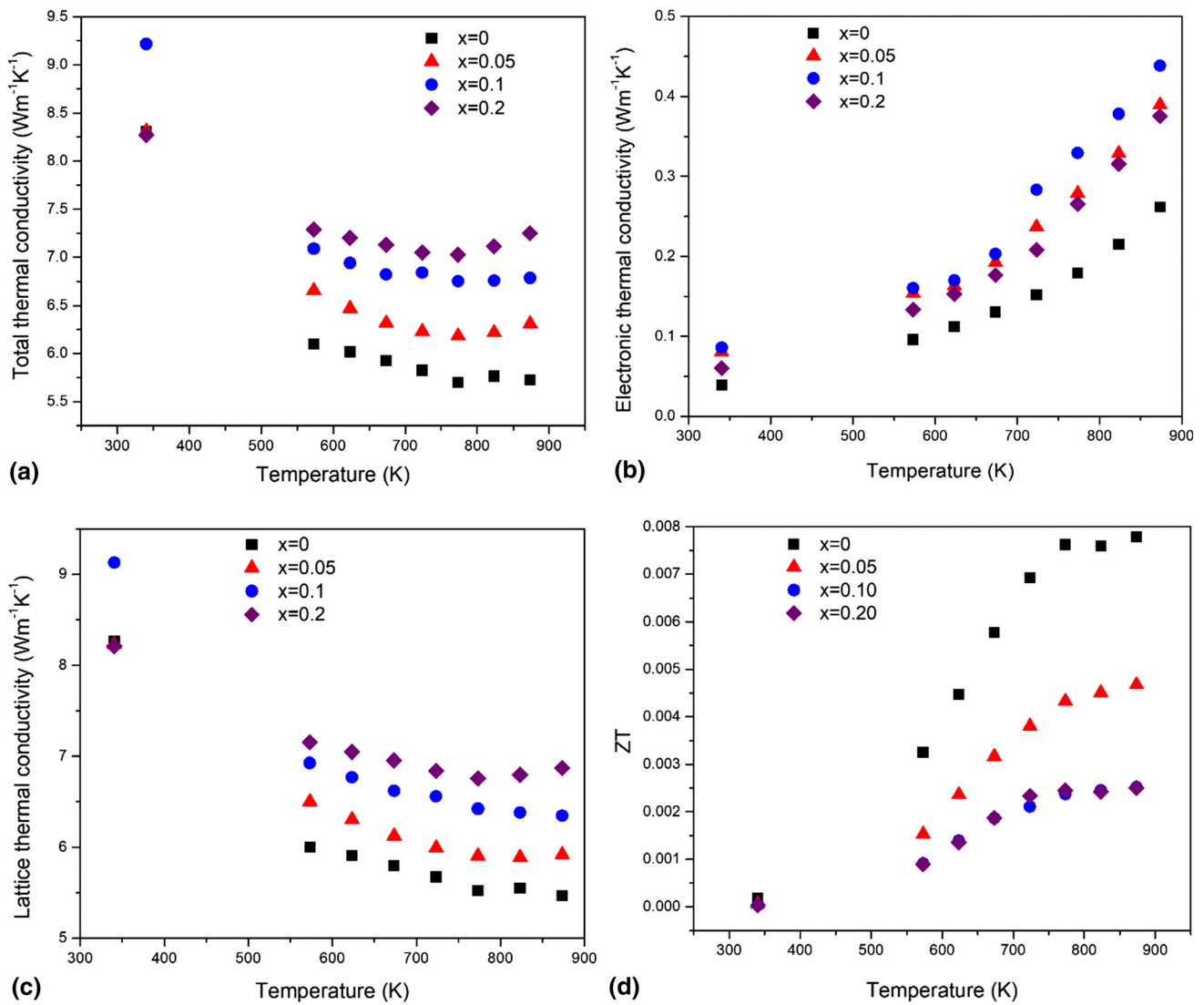
**Fig. 8** (a) Total thermal conductivity, (b) electronic thermal conductivity, (c) lattice thermal conductivity and (d) ZT in 1h BM-SPS $TiFe_{0.5}Ni_{0.5}Sb_{1-x}Sn_x$

the secondary white region could not be determined. As the size of the secondary phases are small ($<1$ $\mu$m), EDS analysis could not give the exact composition of the phase owing to the beam diameter being of similar dimension. However, looking at the BSE micrograph closely, the secondary phase (white) appears to be brighter than the matrix which is grey in color. Thus, it can be assumed that the white region is richer in higher atomic number element, most notably Sb and Sn. However, since there is presence of white region even in the pristine sample, placing the argument of the secondary phase being rich in Sb will not be a wrong assumption. The arguments hold well because in all the compositions, the secondary white region is rich in Sb. It is worth noting that due to inoculation of a greater fraction of secondary phases, the trend of p-type character shown in the $x = 0.2$ alloy in the 1h BM-SPS alloy is not observed for the 5h BM-SPS alloy.

The electrical conductivity as a function of temperature is as displayed in Fig. 9(b). The conductivity value increases with increasing temperature for all the alloys. This implies that the samples are non-degenerate semiconductors. However, the slope change is higher as compared to 1h BM-SPS implying

that the samples are more metallic than the 1h BM-SPS alloys. This is supported by the fact that electrical conductivity of the 5h BM-SPS alloys is one order higher than the 1h BM-SPS alloys. The 5h BM-SPS alloys in addition to the white region has large volume fraction of black region which was found to be TiC (Fig. 6). TiC has an electrical conductivity of $4.7 \times 10^5 Sm^{-1}$ at room temperature. This is one order higher in magnitude than the 1h BM-SPS alloys. This aids in the increase in the electrical conductivity for the 5h BM-SPS alloys. The $x = 0.2$ sample exhibits the minimum electrical conductivity among all the alloys. This can be attributed to the increased volume fraction of secondary phases that leads to charge carrier scattering. The presence of a spike in the electrical conductivity plot for $x = 0.05$ and $x = 0.1$ alloys was observed for the same reason as explained in the 1h BM-SPS alloys.

Although the Seebeck coefficient of the samples is lower, the electrical conductivity of the samples being higher leads to power factor values to be similar in the 5h BM-SPS pellets to the 1h BM-SPS pellets. The overall power factor of the samples decreases with the increase in Sn concentration. A maximum
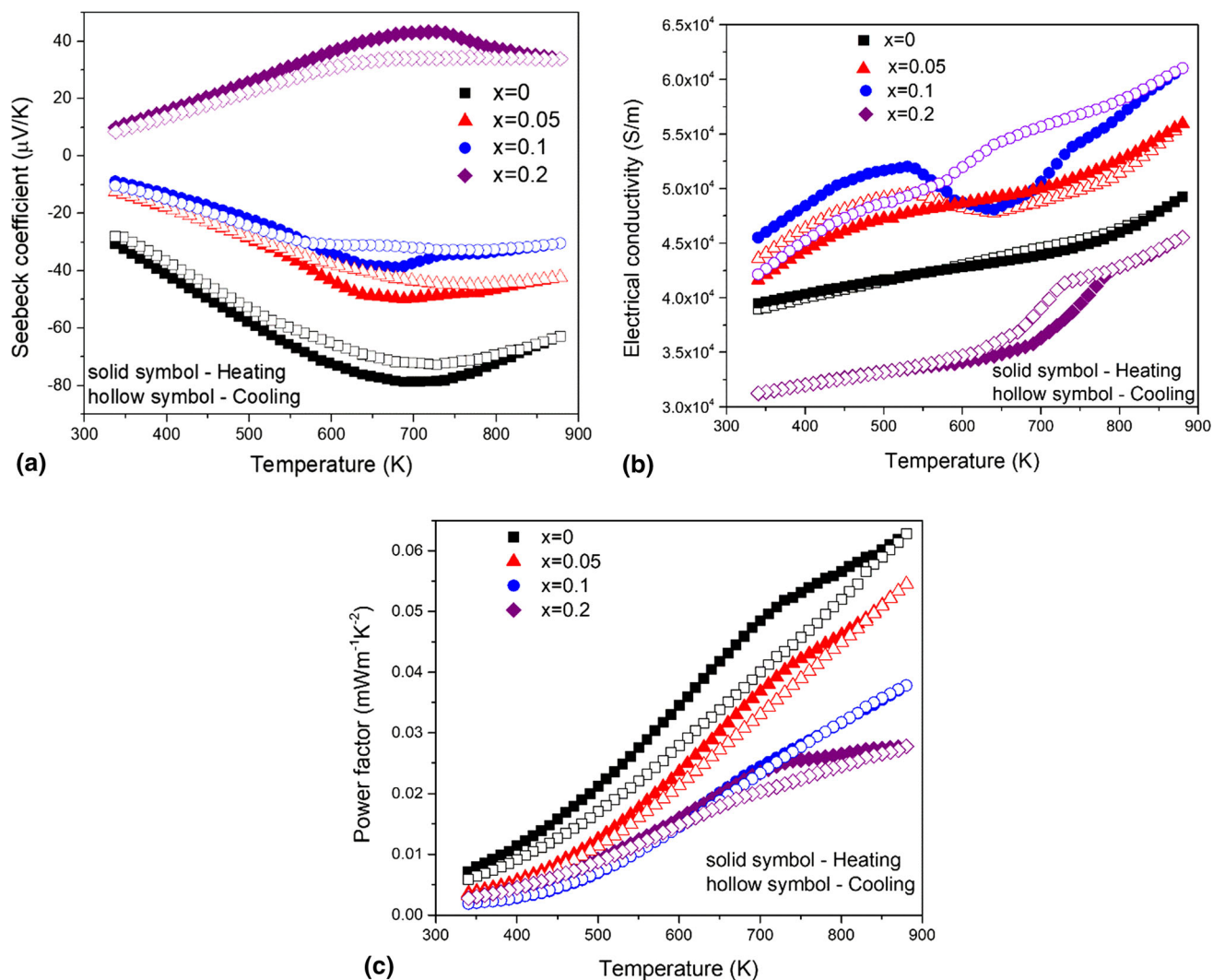
**Fig. 9** (a) Seebeck coefficient, (b) electrical conductivity and (c) power factor of 5h BM-SPS TiFe$_{0.5}$Ni$_{0.5}$Sb$_{1-x}$Sn$_x$

power factor of 0.063 mWm$^{-1}$Ks$^{-2}$ at 880 K was obtained for the pristine sample.

The κ as a function of temperature is displayed in Fig. 10(a). There is a slight increase in κ with increasing temperature. Unlike in the case of 1h BM-SPS alloys, these alloys do not show Umklapp type of scattering. The κ of the x = 0.2 alloy is the largest owing to the presence of a greater volume fraction of TiC. In order to study the contribution of the individual components toward κ, κ$_e$ and κ$_l$ were calculated as shown in Fig. 10(b) and (c), respectively. Owing to the rise in the electrical conductivity value as compared to the 1h BM-SPS pellets, there is an increase in the κ$_e$ in comparison with the 1h BM-SPS pellets. The x = 0.2 alloy shows the lowest κ$_e$ across all temperature and is expected owing to it having the lowest electrical conductivity. The room temperature κ$_l$ of all the samples is lower than the 1h BM-SPS pellets. The 5h BM-SPS pellets are finer in size. This leads to phonon scattering brought about by nanostructuring in the alloys. The κ$_l$ is again the major contributor to the κ in all these alloys. The pristine sample exhibits a maximum ZT = 0.0078 at 873 K. Due to reduced power factor and increased thermal conductivity upon increasing the Sn content, no improvement in ZT value was observed.

## 4. Conclusions

The present work looks into the effect of processing routes on the thermoelectric properties of TiFe$_{0.5}$Ni$_{0.5}$Sb$_{1-x}$Sn$_x$. Vacuum arc melting followed by 1h BM-SPS gave rise to alloys with finer grain size and reduced volume fraction of secondary phases. However, 5h BM-SPS gave rise to increased volume fraction of secondary phases. The power factor of the pristine sample is 0.056 and 0.063 mWm$^{-1}$K$^{-2}$ for the 1h and 5h BM-SPS samples at 873 K. Substitution of Sn in the Sb center led to the decrease in the thermoelectric property due to combined drop in S and rise in κ values. The presence of Sn in the white region confirms that certain Sn goes into the secondary phases and thus complete Sn solubility is not observed after SPS. Furthermore, other than the 20% Sn-doped 1h BM-SPS sample, Sn doping did not bring forth p-type activity in any other alloy. A maximum ZT of 0.0078 at 873 K was obtained for the 1h BM-SPS and 5h BM-SPS undoped samples.
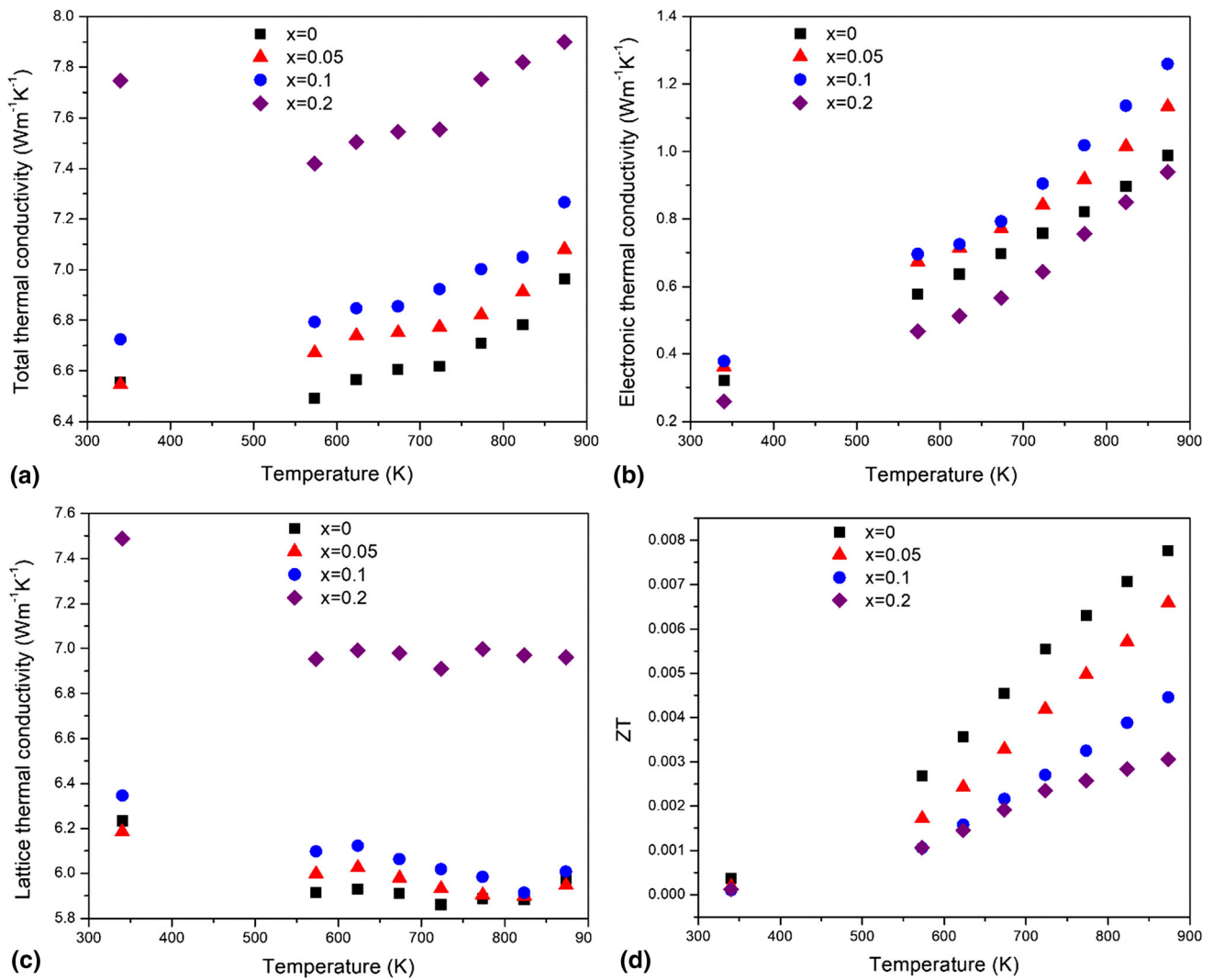
**Fig. 10** (a) Total thermal conductivity, (b) electronic thermal conductivity, (c) lattice thermal conductivity and (d) ZT in 5h BM-SPS $TiFe_{0.5}Ni_{0.5}Sb_{1-x}Sn_x$

## Conflict of interest

The authors declare that they have no conflict of interest.

## References

1. Z.G. Chen, G. Han, L. Yang, L. Cheng and J. Zou, Nanostructured thermoelectric materials: Current research and future challenge, *Prog. Nat. Sci. Mater. Int.*, 2012, **22**, p 535–549

2. R. Fitriani, B.D. Ovik, M.C. Long, M. Barma, M.F.M. Riaz, S.M. Sabri and R. Said, Saidur, A review on nanostructures of high-temperature thermoelectric materials for waste heat recovery, *Renew. Sustain. Energy Rev.*, 2016, **64**, p 635–659

3. D.S. Patil, R.R. Arakerimath and P.V. Walke, Thermoelectric materials and heat exchangers for power generation - A review, *Renew. Sustain. Energy Rev.*, 2018, **95**, p 1–22

4. D.M. Rowe, CRC handbook of thermoelectrics. CRC press, 2018

5. C. Han, Q. Sun, Z. Li and S.X. Dou, Thermoelectric Enhancement of Different Kinds of Metal Ch alcogenides, *Adv. Energy Mater.*, 2016, **6**, p 1600498

6. M. Rull-Bravo, A. Moure, J.F. Fernández and M. Martín-González, Skutterudites as thermoelectric materials: revisited, *RSC Adv.*, 2015, **5**, p 41653–41667

7. E.S. Toberer, A.F. May and G.J. Snyder, Zintl Chemistry for Designing High Efficiency Thermoelectric Materials, *Chem. Mater.*, 2010, **22**, p 624–634

8. G. Rogl, A. Grytsiv, M. Gürth, A. Tavassoli, C. Ebner, A. Wünschek, S. Puchegger, V. Soprunyuk, W. Schranz, E. Bauer, H. Müller, M. Zehetbauer and P. Rogl, Mechanical properties of half-Heusler alloys, *Acta Mater.*, 2016, **107**, p 178–195

9. S. Chen and Z. Ren, Recent progress of half-Heusler for moderate temperature thermoelectric applications, *Mater. Today.*, 2013, **16**, p 387–395

10. W. Jeitschko, Transition metal stannides with MgAgAs and MnCu₂Al type structure, *Met. Trans.*, 1970, **1**, p 3159–3162

11. T. Graf, C. Felser and S.S.P. Parkin, Simple rules for the understanding of Heusler compounds, *Prog. Solid State Chem.*, 2011, **39**, p 1–50

12. Y. Xia, V. Ponnambalam, S. Bhattacharya, A. Pope, S.J. Poon and T.M. Tritt, Electrical transport properties of TiCoSb half-Heusler phases that exhibit high resistivity, *J. Phys. Condens. Matter.*, 2001, **13**, p 77–89

13. T. Sekimoto, K. Kurosaki, H. Muta and S. Yamanaka, Thermoelectric properties of Sn-doped TiCoSb half-Heusler compounds, *J. Alloys Compd.*, 2006, **407**, p 326–329

14. A. Karati, S. Mukherjee, R.C. Mallik, R, Shabadi, B.S. Murty, U.V. Varadaraju, Simultaneous increase in thermopower and electrical conductivity through Ta-doping and nanostructuring in half-heulser TiNiSn alloys, Materialia 7 (2019) 100410

15. X.Y. Huang, Z. Xu and L.D. Chen, The thermoelectric performance of ZrNiSn/ZrO₂ composites, *Solid State Commun.*, 2004, **130**, p 181–185

16. W.J. Xie, J. He, S. Zhu, X.L. Su, S.Y. Wang, T. Holgate, J.W. Graff, V. Ponnambalam, S.J. Poon, X.F. Tang, Q.J. Zhang and T.M. Tritt, Simultaneously optimizing the independent thermoelectric properties in (Ti, Zr, Hf)(Co, Ni)Sb alloy by in situ forming InSb nanoinclusions, *Acta Mater.*, 2010, **58**, p 4705–4713

17. S. Populoh, M.H. Aguirre, O.C. Brunko, K. Galazka, Y. Lu and A. Weidenkaff, High figure of merit in (Ti, Zr, Hf)NiSn half-Heusler alloys, *Scr. Mater.*, 2012, **66**, p 1073–1076

18. I.H. Kim, Y.G. Lee, M.K. Choi and S.C. Ur, Thermoelectric Properties of Half-Heusler $TiCoSb_{1-x}Sn_x$ Synthesized by Mechanical Alloying Process, *Adv. Mater. Res.*, 2013, **660**, p 61–65

19. X. Yan, W. Liu, H. Wang, S. Chen, J. Shiomi, K. Esfarjani, H. Wang, D. Wang, G. Chen, Z. Ren, Stronger phonon scattering by larger differences in atomic mass and size in p-type half-Heuslers $Hf_{1-x}Ti_xCoSb_{0.8}Sn_{0.2}$, Energy Environ. Sci. 5 (2012) 7543

20. S.R. Culp, J.W. Simonson, S.J. Poon, V. Ponnambalam, J. Edwards, T.M. Tritt, (Zr,Hf)Co(Sb,Sn) half-Heusler phases as high-temperature (> 700 °C) p-type thermoelectric materials, Appl. Phys. Lett. 93 (2008) 022105

21. B. Balke, J. Barth, M. Schwall, G.H. Fecher and C. Felser, An alternative approach to improve the thermoelectric properties of half-Heusler compounds, *J. Electron. Mater.*, 2011, **40**, p 702–706

22. J. Toboła, L. Jodin, P. Pecheur, H. Scherrer, G. Venturini, B. Malaman, S. Kaprzyk, Composition-induced metal-semiconductor-metal cross-over in half-Heusler $Fe_{1-x}Ni_xTiSb$, Phys. Rev. B - Condens. Matter Mater. Phys. 64 (2001) 1551031-1551037

23. K. Kutorasinski, J. Tobola and S. Kaprzyk, Application of Boltzmann transport theory to disordered thermoelectric materials: Ti(Fe Co, Ni)Sb half-Heusler alloys, *Phys. Status Solidi Appl. Mater. Sci.*, 2014, **211**, p 1229–1234

24. J. Toboła, J. Pierre, S. Kaprzyk, R.V. Skolozdra and M.A. Kouacou, Crossover from semiconductor to magnetic metal in semi-Heusler phases as a function of valence electron concentration, *J. Phys.: Condens. Matter*, 1998, **10**, p 1013–1032

25. E. Rausch, B. Balke, S. Ouardi, C. Felser, Enhanced thermoelectric performance in the p-type half-Heusler $(Ti/Zr/Hf)CoSb_{0.8}Sn_{0.2}$ system via phase separation. Phys. Chem. Chem. Phys. 16 (2014) 25258-62

26. A. Karati, M. Vaidya and B.S. Murty, Comparison of different processing routes for the synthesis of semiconducting AlSb, *J. Mater. Eng. Perform.*, 2018, **27**, p 6196–6205

27. A. Karati, M. Nagini, S. Ghosh, R. Shabadi, K.G. Pradeep, R.C. Mallik, B.S. Murty and U.V. Varadaraju, Ti2NiCoSnSb-a new half-Heusler type high-entropy alloy showing simultaneous increase in Seebeck coefficient and electrical conductivity for thermoelectric applications, *Sci. Rep.*, 2019, **9**, p 5331-1–12

28. A. Karati, V.S. Hariharan, S. Ghosh, A. Prasad, M. Nagini, K. Guruvidyathri, R.C. Mallik, R. Shabadi, L. Bichler, B.S. Murty and U.V. Varadaraju, Thermoelectric properties of half-Heusler high-entropy Ti2NiCoSn1-xSb1+x (x = 0.5, 1) alloys with VEC > 18, *Scr. Mater.*, 2020, **186**, p 375–380

29. T.B. Massalski, H. Okamoto, P.R. Subramanian, L. Kacprzak and W.W. Scott, *Binary Alloy Phase Diagrams Metals Park*, American society for metals, OH, 1986

30. T. Sekimoto, K. Kurosaki, H. Muta and S. Yamanaka, Annealing effect on thermoelectric properties of TiCoSb half-Heusler compound, *J. Alloys Compd.*, 2005, **394**, p 122–125

31. S. Tippireddy, D.S.P. Kumar, A. Karati, R. Anbalagan, P. Malar, K.H. Chen, B.S. Murty and R.C. Mallik, The effect of Sn substitution on the thermoelectric properties of synthetic tetrahedrite, *ACS Appl. Mater. Interfaces.*, 2019, **11**, p 21686–21696

32. J.V. Hoch, Michael, Thermal conductivity of TiC, *J. Am. Ceram. Soc.*, 1963, **46**, p 245–245

33. B. Liao, S. Lee, K. Esfarjani and G. Chen, First-principles study of thermal transport in $FeSb_2$, *Phys. Rev. B.*, 2014, **89**, p 35108